Surrogate model based design optimization of multiple wing sails considering flow interaction effect

Hakjin Lee[a], Yeongmin Jo[a], Duck-Joo Lee[a], and Seongim Choi[b, *]

[a] *Department of Aerospace Engineering, Korea Advanced Institute of Science and Technology (KAIST), Daejeon 305-701, Republic of Korea*

[b] *Department of Aerospace and Ocean Engineering, Virginia Polytechnic Institute and State University, Blacksburg, 24061, VA, U.S.A*

Abstract

The purpose of our study is to numerically analyze the aerodynamic characteristics of multiple wing sails which have three identical wing sails in a row and optimize their shape and operation conditions in terms of the flap length, deflection angle and angle of attack under various wind directions. A viscous Navier-Stokes flow solver is used for the numerical aerodynamic analysis. A design optimization framework using an evolutionary algorithm and the Kriging surrogate model is developed and finds the optimum solution for multiple wing sails to maximize the thrust coefficient. A total of nine design variables are employed, and relative wind direction, which is allowed to vary from 45° to 90° and 135°. The design results are validated using a three-dimensional Computational Fluid Dynamics analysis. The validation results show that the average thrust performance of optimized multiple wing sails was improved in all wind directions in comparison with the baseline multiple wing sails.

Keywords: Wind assisted propulsion system, Wing sail, Computational Fluid Dynamics (CFD), Design optimization, Genetic Algorithm (GA), Kriging surrogate model

Nomenclature

C_L	=	lift coefficient
C_D	=	drag coefficient
C_P	=	surface pressure coefficient
C_{Fx}	=	thrust force coefficient in the x direction
C_{Fy}	=	side force coefficient in the y direction

* Corresponding author. E-mail address: schoi1@vt.edu

$C_{Fx.avg}$	=	averaged thrust force coefficient in the x direction
I	=	objective function
α_i	=	angle of attack (degree)
α_{lower}	=	lower limit of angle of attack (degree)
α_{upper}	=	upper limit of angle of attack (degree)
δ_i	=	flap deflection angle (degree)
δ_{lower}	=	lower limit of flap deflection angle (degree)
δ_{upper}	=	upper limit of flap deflection angle (degree)
$X_{flap,i}$	=	flap length (meter)
$X_{flap,lower}$	=	lower limit of flap length (meter)
$X_{flap,upper}$	=	upper limit of flap length (meter)
θ	=	apparent wind direction (degree)
n	=	the number of sampling
d	=	the number of design variables
k	=	the order of basis function in Kriging model
$\hat{y}$	=	estimated response in Kriging model
$\mathbf{x}$	=	design variables
$f(\mathbf{x})$	=	trend (drift) term of Kriging model
$Z(\mathbf{x})$	=	deviation term of Kriging model
$f_i(\mathbf{x})$	=	basis function
β_i	=	basis function coefficient
$\mathbf{y}$	=	response vector of samplings
$\mathbf{F}$	=	basis function matrix
$\mathbf{f_x}$	=	basis function vector
$\mathbf{R}$	=	correlation matrix
$\mathbf{r_x}$	=	correlation vector
$R(x_i, x_j)$	=	correlation function
σ_z^2	=	variance of Gaussian random process
$\hat{\boldsymbol{\beta}}$	=	estimated coefficient of basis function
θ_k	=	parameter of correlation function
p	=	parameter of correlation function
$L(\theta_k)$	=	maximum likelihood estimation (MLE) of θ_k

Acronyms

AoA	=	Angle of Attack
AWS	=	Apparent Wind Speed
AWA	=	Apparent Wind Angle
CFD	=	Computational Fluid Dynamics
DOE	=	Design of Experiment

EA	=	Evolutionary Algorithm
GA	=	Genetic Algorithm
LHS	=	Latin Hypercube Sampling
MLE	=	Maximum Likelihood Estimation
MSE	=	Mean Square Error
RANS	=	Reynolds Averaged Navier-Stokes
SA	=	Spalart-Allmaras

1. Introduction

Energy is becoming a pressing issue in industry and academia because energy consumption has been growing continuously and is focused mainly on fossil fuels, which create environmental pollution. A study on an eco-friendly energy source as an alternative to fossil fuels is actively sought in all engineering fields. In the ship industry, a conventional propulsion system greatly relies on fossil fuels and the emission of pollutants causes great problems in the ocean system. Therefore, the new propulsion technologies have been developed that can replace or support existing reciprocating and turbine engines based on fossil fuels. In recent years with increased focus on reducing emission of carbon dioxide (CO_2) and increasing fossil fuel costs, a wind assisted propulsion systems have been attempting to apply on the commercial ships. The wind assisted propulsion systems, such as regular soft sails, wing sails, kite sails, and Flettner rotor use the wind energy that is eco-friendly alternative energy sources to produce an additional propulsive force. Converting the kinetic energy of wind into thrust for the ship is the basic concept of the wind assisted propulsion systems. The kite sails system consists of a flying large kite and an automatic control system to determine the kite position. It is easy to install for the existing ship with low cost. On the other hand, a rotor ship, or Flettner ship uses rotating cylinders that are mounted on deck of ship to produce the additional propulsion force. The thrust force is generated by rotating cylinder in a moving fluid flow due to Magnus effect that is used to proper the ship. The wing sails that are mounted on the deck of ship catch the kinetic energy from the wind and assist in pulling the ship. The basic concept of wing sail is to enhance the existing propulsion efficient by using the aerodynamic propulsion provided by wing sails which utilize the same shape as the wing of an airplane rather than regular soft sails. Recent research results reached the conclusion that more than 15 ~ 25 % of the existing propulsion force can be replaced with wing sails, leading to a saving of an equivalent proportion of fossil fuels (Kazuyuki Ouchi et al. 2011).

Research on wing sails has been conducted by many groups. Kazuyuki Ouchi et al. (2011) performed the aerodynamic and structure analyses of multiple wing sails using numerical methods. Toshifumi Fujiwara et al. (2003)

studied the aerodynamic characteristics of multiple wing sails with respect to the angle of the boom and slot. Furthermore, Toshifumi Fujiwara et al. (2005) carried out a wind tunnel experiment to reveal the sail-sail and sail-hull interaction effects. Takuji Nakashima et al. (2009) also conducted a wind tunnel measurement and numerical simulation to clarify the aerodynamic interaction phenomena between wing sails in a new conceptual wind-driven vessel. Qiao Li et al. (2015) investigated the best setup parameters and analyzed the aerodynamics interaction of the proposed a new wing sail in the wind tunnel and the numerical simulation. However, most of these studies only focused on the aerodynamic analysis of the wing sails and depended on wind tunnel experiments. Not much attention has been given to the design optimization aspect to improve the aerodynamic performance of wing sails. In the present study, we developed the design optimization framework, which is tightly coupled with numerical analysis and optimization algorithms and conducted the design optimization to enhance the aerodynamic propulsion force provided by wing sails.

In this study, we conduct an aerodynamic analysis to investigate the effects of the flow interactions and aerodynamic characteristics of the multiple wing sails using Computational Fluid Dynamics (CFD) flow solvers. A viscous Navier-Stokes solver is used with an unstructured mesh topology for both two- and three-dimensional numerical analyses of the multiple wing sails. The turbulence model of Spalart-Allmaras (SA) is employed. The magnitude of the propulsive force is investigated for the wing sails both with and without the flap, while the wind direction is allowed to vary from 0° to 360° in 15° steps. To validate the accuracy of the CFD solver for the current flow conditions of the wing sails, a two-dimensional flow analysis is conducted around the NACA 0012 airfoil, and the results are compared with the experimental values. Next, the highly accurate flow solutions are directly used for aerodynamic design optimization in consideration of flow interactions in the multiple wing sails. A key advantage of our work is conduction of a trade-off study of the design parameters that are known to be effective in improving the wing sail performance. We find the optimum topology of the multiple wing sails in terms of the operation condition and flap configurations. An aerodynamic design optimization framework for multiple wing sails is developed. This framework uses evolutionary algorithms and the Kriging surrogate model and is fully automated. We also carry out the CFD-based design optimization using a continuous adjoint method tightly coupled with the CFD solver and adjoint solver. However, it is difficult to smoothly handle the mesh deformation, because we consider the operating condition as well as the flap configuration as design variables. Using developed design framework, we find the optimal setup for the multiple wing sails to maximize the averaged thrust coefficient and thus increase the overall propulsive force. A total of nine design variables are employed, and each wing sail has design parameters for varying the angle of attack of the wing sail and the flap configurations in terms of the length and its deflection angles. In our previous study, we only considered the variation in the angle of attack of each wing sail as design variables that could be rotated up to ± 15° independently (Lee, 2012). However, in this study, we consider not only the angle of attack but also the flap length and deflection angle of each wing sail as design variables. Finally, the optimal design variables are obtained to maximize the averaged thrust performance of the multiple wing sails, and the apparent wind direction is allowed to vary from 45° to 90° and 135°. As a result, we achieve a thrust improvement of approximately 14 ~ 22 % at the initial angle of attack of 8°. Although the design is carried out based on the two-dimensional flow analysis, mostly because of the expensive computational cost, a validation is carried out with the complete three-dimensional wing sails using a CFD analysis to determine whether the thrust improvement achieved from the two-dimensional assumption is valid. The results show that the thrust performance improvement in the multiple wing sails becomes slightly lower in the three-dimensional analysis, which is very predictable considering the three-dimensional aerodynamic effects, including the downwash flow due to wing tip vortex, and cross-flows etc.

In conclusion, our work has advantages of providing information useful for understanding the aerodynamic characteristics of wing sails and of determining the optimum setup for multiple wing sails under various operation conditions. Our work indicates that the concept of wing sails is a valid and viable tool that can serve as an efficient alternative propulsion system in the ship industry. However, we have some limitations in this research. First, we do not consider the wind shear effect. Actually the wind speed at greater altitudes is faster than the ground or water surface due to viscosity. Therefore, the wind speed has to be changed along the height of wing sail. However, the uniform wind speed distribution along the height of wing sail was used in this study. Second, we focus only on the wing sails and flow interaction effect among them. Therefore we do not consider a hull model and the interaction effect of sail-hull or other ship superstructures. Third, we assume that the ship with wing sails can move only one-direction (x-axis direction) regardless of wind direction. The direction of thrust force acting on wing sails is also defined along the ship moving direction (x-axis direction) to propel the ship. The effect of side force that result from normal force acting on wing sails is ignored in this study. Fourth, in the present work, the simplified shape of wing sail was used for wind-assisted propulsion system. It is a rectangular wing with no twist and no sweep back angle and its section is made of NACA 0012 symmetric airfoil with a flap. The flap is modeled without any gap. The multi-element rigid wing sails, hybrid-sail with slat and square soft sail, and large vertically retractable rigid sail have been modeled and suggested as the wind-assisted propulsion system. The multi-element rigid wing sails were composed of two different airfoils with a small gap in between, and can generate higher lift force than curved plates (Ignazio Maria Viola et al., 2015). The hybrid-sail consisted rigid wing sail of NACA 0030 form as a mast with slat of a circular arc and square soft sail for high aerodynamic performance (Toshifumi Fujiwara et al., 2003). The retractable rigid sail can vertically fold and has a self-rotating mechanism to meet the wind direction (Kazuyuki Ouch et al., 2013).

The outline of this paper is as follows. Section II introduces the concept of wing sails, topology of multiple wing sails, and force relation for evaluating the thrust performance. Sections III and IV respectively describe the aerodynamic analysis method and design optimization framework. Section IV discusses the Kriging approach for surrogate modeling, as well as the GA employed in this study. Section V explains the aerodynamic characteristics and flow interaction of multiple wing sails. Section VI then shows the results of the aerodynamic design optimization, initially at an angle of attack of 8° in consideration of the flow interaction, as mentioned in Section V. Section VII concludes this paper.

2. Concept of wing sails

The ship with wing sails is an eco-friendly and fuel-efficient vessel that uses wing sails to support an existing fossil fuel based propulsion system. The wing sails catch the kinetic energy from the wind and produce an additional thrust force to assist in pulling the ship. The “Shin-Aitoku Maru” was the first sailing ship to use a large hard wing sail propulsion system. It was introduced by JAMDA Japan in the 1970s. At first, simple flat-type sails were applied. Then, the sailing ship was developed, which utilized sails with an airfoil shape instead of the flat-type of sail. This considerably improved the aerodynamic performances of the wing sails.

The wing sails have to be located in the limited space available on the main deck. The number of wing sails is generally determined by the size of the ship (Takuji Nakashima et al. 2011). In a previous study, a wing sail system with a total of six sails was considered for a cargo ship in the 100-K DWT (Dead Weight Tons) class (Lee et al., 2012). In this study, we consider a wing sail system with three sails for a cargo ship in the 50-K DWT class. The reduction in the number of wing sails in the present study is based on the observation that the most dynamic flow interaction occurs in the area of the first three wing sails (Lee et al., 2012). **(Figure 1)** shows a schematic of the wing sail system being considered here. Each wing sail has a chord length of 10 m, height of 20 m, and aspect ratio of 2 without any taper and twist. In addition, the interval between the wing sails is 15 m, which is 1.5 times the chord length. The three wing sails are arranged along the *x* direction. The wing sails can rotate to face various wind directions, and the axis of rotation is located at 40 % of each chord length. The sectional shape of the wing sails is an NACA 0012 airfoil, which is symmetric and does not have a camber. The reason for selecting the symmetric airfoil is to prevent the negative camber effects on the aerodynamic performance because the wind direction can vary from 0° to 360° during a cruise mission. As shown in **(Figure 1),** if the wing sails are constructed as multiple arrangements in a row to generate more thrust, a flow interaction occurs among them, and it has a significant effect on the overall propulsion performance of the multiple wing sails. Therefore, the effect of this flow interaction should be considered in order to accurately estimate the thrust of multiple wing sails.

(Figure 2) shows a force diagram representing the sail direction, apparent wind direction, and force coefficients acting on the wing sail. Consider that the ship is being propelled only in *x*-direction. Then, the resultant force along the *x*-direction, which is thrust force coefficient (C_{Fx}), can be calculated using Eq. (1). The formulation of the thrust vector can be defined as a function of the apparent wind direction (θ) and aerodynamic coefficients (C_L, C_D) of the wing sail. The total aerodynamic force acting on wing sail can be resolved into lift and drag force based on the apparent wind direction or thrust (driving force) and side force (lateral force) based on the direction the ship is travelling. Thrust and side force coefficient both along the x and y directions can be calculated using Eq. (1) and Eq. (2). In the ship using wind-assisted propulsion system, the side force is as important as the thrust force because it must be balanced by a hydrodynamic side force, which is generated by the hull and appendages. The higher side force is generated by the wing sail, the more hydrodynamic side force generated by the fin keels or rudder is needed to resist the aerodynamic force. The leeway angle has to be increased to balance the two side forces. However, this leads to a significant increase in the hull resistance. The yaw moment generated due to the aerodynamic and hydrodynamic side force will be balanced by the moment produced by the rudder. Therefore, the synthetic evaluation in consideration of side forces and moments is significant because it can directly affects ship performance. However, that requires information on detailed ship geometry with CAD representation including hull form, propellers, rudders, and other appendages, which are not readily available in the current study. Computation time for the CFD simulation of entire ship throughout design iterations becomes prohibitively expensive. A high-level, multidisciplinary design optimization framework is needed with careful choices on the constraints and design variables. Although those can be done in future work, the scope of the current study is limited to isolated wing sails and focused on how effectively the CFD-based flow analysis and design are used to computation the variation of a performance metric, a thrust level, for example in our work, with respect to wind direction, angle of attack of wing sails, and flap topology. For multiple wing sails, the average thrust is considered to be a performance indicator, and it is an average thrust coefficient divided by the number of wing sails. In this study, a wing sail system with three sails is considered. Thus, the averaged thrust coefficient is defined as Eq. (3).

$$C_{fx} = C_L \sin\theta - C_D \cos\theta \qquad \text{Eq. (1)}$$

$$C_{fy} = C_L \cos\theta + C_D \sin\theta \qquad \text{Eq. (2)}$$

$$C_{fx.avg} = \frac{1}{3}\sum_{i=3}^{3} C_{fx,i} \qquad \text{Eq. (3)}$$

3. Aerodynamic analysis methods

3.1 Computational Fluid Dynamics (CFD)

In order to investigate the flow phenomena, an appropriate CFD flow solver must be selected. SU2_CFD is fluid dynamics software for simulations in a parallel computation environment, along with a module for partitioning the volumetric grid as a pre-processor in parallel flow computations. SU2_CFD solver can provide direct flow solutions and adjoint solutions for potential, Euler, Navier-Stokes, and Reynolds Averaged Navier-Stokes (RANS) governing equations. It uses a Finite Volume Method (FVM) for spatial discretization. Both explicit and implicit methods are available for time integrations, and central difference or upwind methods can also be used for spatial discretization. To improve the robustness and convergence of the flow solution, the advanced numerical techniques of residual smoothing and agglomeration multi-grid methods are also available. SU2_CFD code has been verified and validated through various test cases, including steady and unsteady Euler and RANS, multi-species and non-equilibrium flow, low-speed (low Mach number) and supersonic simulation (Alonso and Colonno, 2012), free surface formulation (Palacios et al. 2012), Time-accurate simulation with dynamic mesh (Colonno et al. 2012), or plasma simulation (Palacios et al. 2013). SU2_CFD also can be used to solve a variety of design optimization problem such as supersonic aircraft using equivalent area distributions (Lukaczyk et al. 2012), wing design with RANS equation and continuous adjoint approach (Bueno-Rrovio et al. 2012) and optimal shape design for rotor in hover (Economon et al. 2012).

For the numerical analysis, we solve the two- and three-dimensional compressible RANS governing equations, which describe the conservation of mass, momentum, and energy in a viscous fluid. These governing equations have the following structure in differential form:

$$\partial_t \mathbf{U} + \nabla \cdot \mathbf{F}^c - \nabla \cdot \mathbf{F}^v = \mathbf{Q} \quad in\ \Omega \in \mathbf{R}^3, t > 0 \qquad \text{Eq. (4)}$$

where t is the time and Ω is the domain. $\mathbf{U}$ denotes the vector of state variables; $\mathbf{F}^c$ are the convective fluxes (inviscid fluxes); $\mathbf{F}^v$ are the viscous fluxes; and $\mathbf{Q}$ is a source term. Eqs. (5) and (6) give a brief description of the physics involved for each component of the governing equations:

$$\mathbf{U} = \left(\rho, \rho v_1, \rho v_2, \rho v_3, \rho E\right)^T \qquad \text{Eq. (5)}$$

$$\mathbf{F}^c = \begin{pmatrix} \rho v_i \\ \rho v_i v_1 + P\delta_{i3} \\ \rho v_i v_2 + P\delta_{i3} \\ \rho v_i v_3 + P\delta_{i3} \\ \rho v_i E \end{pmatrix}, \quad \mathbf{F}^v = \begin{pmatrix} 0 \\ \tau_{i1} \\ \tau_{i2} \\ \tau_{i3} \\ v_j \tau_{ij} + \mu_{tot}^* C_p \partial_i T \end{pmatrix}, \quad i = 1 \cdots 3 \qquad \text{Eq. (6)}$$

where ρ is the density, P is the static pressure, E is the total energy per unit mass, H is the fluid enthalpy, and $\vec{v} = (v_1, v_2, v_3) \in \mathbf{R}^3$ is the flow velocity vector in a Cartesian coordinate system. In these formulations, the static pressure P could be derived from the state equation with the assumption of an ideal gas.

$$P = \rho(\gamma - 1)[E - \frac{1}{2}(v_1^2 + v_2^2 + v_3^2)] \qquad \text{Eq. (7)}$$

$$T = \frac{P}{R\rho}, \quad C_P = \frac{\gamma R}{(\gamma - 1)} \qquad \text{Eq. (8)}$$

where T is the temperature, γ is the specific heat ratio, and R is a gas constant. C_P is the specific heat at a constant pressure, and δ_{ij} is the Kronecker delta function. For the viscous flux term of Eq. (6), the viscous stresses can be written as Eq. (9). The viscosity is defined by Stokes' assumption.

$$\tau_{ij} = \mu_{tot}(\partial_j v_i + \partial_i v_j - \frac{2}{3}\delta_{ij} \nabla \cdot \vec{v}) \qquad \text{Eq. (9)}$$

$$\mu_{tot} = \mu_{dyn} + \mu_{tur}, \quad \mu_{tot}^* = \frac{\mu_{dyn}}{\mathrm{Pr}_d} + \frac{\mu_{tur}}{\mathrm{Pr}_t} \qquad \text{Eq. (10)}$$

The dynamic viscosity (molecular laminar viscosity) μ_{dyn} is derived using Sutherland's Law (White, 1974), and the turbulent viscosity μ_{tur} is calculated using a turbulence model. In the present paper, we use the one-equation turbulence model of Spalart-Allmaras (SA) to compute turbulent viscosity μ_{tur}. The Prandtl numbers for laminar (Pr_d) and turbulent (Pr_t) flows, which have values set at 0.72 and 0.9, respectively.

3.2 Numerical schemes

To solve the governing equation of Partial Differential Equation (PDEs) form, the spatial terms of the governing equations should be discretized by using the Finite Volume Method (FVM) or Finite Difference Method (FDM). In general, there are two strategies for finite volume discretization. One way is cell-centered based FVM. Another way is cell-vertex based FVM. In cell-centered based FVM, the control volumes are the cell themselves, and the flow variables are stored in centroid of each cell. Otherwise, in cell-vertex based FVM, the control volumes are comprised of sub-finite volume, and the flow variables are stored in the cell vertices or nodes. In our study, the spatial terms of the governing equations are discretized using the cell-vertex (node) based FVM with a Median Dual control volume technique. This technique uses the centroid point of cell and midpoint of the edge of triangular unstructured mesh to construct the virtual control volume. The inviscid and viscous flux terms are evaluated using the central difference scheme, which is second-order accuracy in space. The central difference scheme is easier to implement and requires less computing costs than the upwind difference scheme. Moreover, we use the Jameson-Schmidt-Turkel (JST) scheme as an artificial viscosity term for obtaining high-resolution solution and preventing non-physical oscillation errors (Jameson, 1995). In order to obtain a steady-state solution, we perform pseudo-time integration using the Lower-Upper Symmetric Gauss Seidel (LU-SGS) scheme (Yoon and Jameson, 1988). As we mentioned before, the SA turbulent model is used to calculate the turbulent viscosity. We employed the local-time-stepping technique and multigrid method to accelerate the convergence of steady-state solution. The local-time-stepping technique allows each cell to use a different time step that is determined by the Courant-Friedrich-Lewy (CFL) stability condition. The local time step for stability is calculated by using the eigenvalues and the first-order approximations to the Jacobians at every node (Palacios, 2013). The multigrid method is also considered as convergence acceleration techniques. It was suggested in the 1960's by Fedorenko (1962) and Bakhvalov (1966) to solve an elliptic boundary-value problem. Nowadays, multigrid is used as standard acceleration technique for the solution of the Navier-Stokes equation (Blazek, 2011).

3.3 Computational gird, boundary and flow conditions

For the numerical analysis, the physical domain has to be discretized with the small spacing cells as shown in **(Figure 3)**. In addition, the size of physical domain is restricted on the artificial boundaries. The size of the computational domain is 45 (x-direction) × 15 (y-direction) × 30 (z-direction) times the chord length. The x, y, and z-axis direction correspond with the streamwise, spanwise and cross-streamwise direction respectively. The total number of node and elements for computational mesh is list in **(Table 1)**.

In order to obtain the accurate numerical solution close to the real flow solution, it is significant to apply the proper boundary conditions. At the solid surface, a relative velocity between the solid surface and the fluid on the surface is zero due to the viscosity of fluid. It is called no-slip conditions. We employed the no-slip boundary condition as viscous wall boundary condition near wing sails surface to consider this effect of viscous. At the artificial far-field boundaries and the root plane of wing sails where the wing sails were mounted on the deck, the far-field and symmetry boundary condition were used respectively. The far-field boundary condition prevents the reflected disturbances to come back within the boundaries. There is no flow across the boundary at root plane of wing sails due to symmetry boundary condition.

The Reynolds number based on the chord length of wing sail is set to 10,000,000. The apparent wind speed (AWS) between true wind speed and ship cruse speed is 14 knots (7 m/s). In this study, the flow around the multiple wing sails has a very low speed. In this velocity region, it is important to consider the viscous effect for a more accurate flow solution. Because of the viscous effect on the wall, a boundary layer flow is developed and has to be accurately captured. If we do not use a wall function in the turbulence model, a high-resolution mesh is required near the wall with the value of y+ close to unity. In the unstructured grid methodology, the mixed grids are generally utilized for the viscous computation. A mixed grid of quadrangles and triangles is used in the two-dimensional mesh, and a combination of hexahedrons and tetrahedrons is used for the three-dimensional mesh topology. The mixed grid topology for our multiple wing sails configuration is shown in **(Figure 3)**.

4. Design optimization methods

In addition to the aerodynamic analysis of the multiple wing sails, we developed a design optimization framework, which is tightly coupled with the flow analysis and gradient-free optimization algorithms. In this section, we explain two components of the current design optimization framework: Kriging surrogate model and Genetic Algorithm (GA). We also introduce a fully automated design optimization framework that integrates the geometry kernel, mesh generation, deformation, flow solution, and optimization algorithm.

4.1 Evolutionary algorithm

Evolutionary algorithms (EAs) were inspired by the processes involved in the natural evolution of humans, including inheritance, mutation, selection, and crossover. Because EAs do not require gradient information, they are used widely for many problems in which gradient information is very difficult to compute. The Genetic Algorithm (GA), Memetic Algorithm (MA), and Neuro-evolution are typical examples of EAs. The GA is one of the most popular EAs. The GA is particularly attractive because it does not require gradient-based sensitivity information and is very robust and effective at finding the global optimum. Furthermore, the GA searches the entire design space and is less likely to get stuck at the local optimum than the gradient-based design optimization method. When the design space is defined, the GA randomly selects a population set. The function evaluation must be performed for every candidate in the population set to compare a fitness of each candidate. Then, the genetic operators select better candidates as an inheritance set for the next generation and also create the new candidates that shares many of the characteristics of candidates in the previous generation through a combination of mutation and crossover. Then, the more evolved candidates will survive through the generations. After many generations, the best one is chosen as the optimal solution. Commonly, these iterative generations are repeated until either the fixed number of generation are reached, or the optimal solution is found that satisfies the termination criteria (Pham, 1995). As shown in **(Table 2),** the number of generation and population and the probability of mutation and crossover were determined by the user.

However, the GA requires a large number of function evaluations in each generation. Therefore, we employ the Kriging surrogate model, which is an interpolation-based surrogate model to alleviate the computational cost of the optimization algorithm related to the large number of function evaluations. The Kriging surrogate model is created by evaluating an initial sampling set of function evaluations through Navier-Stokes flow solver.

4.2 Kriging surrogate model

The gradient-free optimization algorithms such as the GA are known to be easy and robust methods for finding the optimal solution. However, the objective function should be evaluated for every member in the population at each generation. If we use the CFD computation for the function evaluation, it is practically impossible to apply GA directly to a design problem, because a single function evaluation may take a couple of hours, even with parallel computation. For this reason, a surrogate model or response surface method is introduced in order to substitute the function evaluation. The surrogate model, known as an approximate model, is an efficient way of alleviating the expensive computation burden in the design optimization. The function evaluation of the initial experimental sample points is only required to construct the surrogate model. The experimental sample points are randomly selected in the design space. After the surrogate model is constructed, we can obtain any approximated value of the objective function from the surrogate model without additional function evaluations within one seconds.

There are two types of surrogate models. The polynomial-based regression model usually uses a least-squares method to emulate the trend of a real function. This regression technique focuses on estimating the relationships among function values and the trend of these values. Therefore, this approach is very sensitive to the distribution of data and does not guarantee that the resulting regression surface passes through all the sample data points (Yi et al. 2012). On the other hand, another surrogate model method uses a data-fitting technique, which is known as an interpolation. This interpolation-based surrogate model can construct the response surface that always passes through all the initial sampling points by using interpolation between the data points. For this reason, the interpolation-based surrogate model is known to be good for noisy and nonlinear results such as CFD simulation. In this study, we use the Kriging surrogate model, which is the interpolation-based surrogated model and popularly used in combination with the gradient-free methods. The Kriging surrogate model is defined as the sum of the mean and deviation terms, as shown in Eq. (11). The mean represents an approximate trend of the real function. The deviation term is a quantified value that is the difference between the real function and the approximated function. In other words, it is an error term.

$$\hat{y}(\mathbf{x}) = f(\mathbf{x}) + Z(\mathbf{x}) \quad \text{Eq. (11)}$$

The mean term can be rewritten as a combination of the basis function and its coefficients, as shown in Eq. (12). The coefficients are able to be determined by Generalized Least Square (GLS) (Kurganov and Levy, 2003).

$$\hat{y}(\mathbf{x}) = \sum_{j=1}^{k} \beta_j f_j(\mathbf{x}) + Z(\mathbf{x}) \quad \text{Eq. (12)}$$

The Kriging model can be classified as an ordinary, universal, or Taylor-Kriging model depending on the method used to formulate the mean term using polynomial equations. If we can predict the trend of the real function, the universal and Taylor-Kriging models are very useful approaches. In general engineering problems, because we do not know the exact trend for the real function, the ordinary Kriging model is mainly used. In the ordinary Kriging model, the polynomial trend term in Eq. (11) is considered to be a constant, namely, the 0^{th}-order polynomial equation. Therefore, the ordinary Kriging model has the advantage of robust behavior for any problem (Journel and Rossi, 1988 and Zimmerman et al. 1999).

$$\mathbf{y} = [y(\mathbf{x_1}), y(\mathbf{x_2}), \cdots, y(\mathbf{x_n})]^T \quad \text{Eq. (13)}$$

$$\mathbf{f_x} = [f_1(\mathbf{x}), f_2(\mathbf{x}), \cdots, f_k(\mathbf{x})]^T \quad \text{Eq. (14)}$$

$$\mathbf{F} = \begin{bmatrix} f_1(\mathbf{x_1}) & f_2(\mathbf{x_1}) & \cdots & f_k(\mathbf{x_1}) \\ f_1(\mathbf{x}_2) & f_2(\mathbf{x}_2) & \cdots & f_k(\mathbf{x}_2) \\ \vdots & & \ddots & \\ f_1(\mathbf{x}_k) & f_2(\mathbf{x}_k) & \cdots & f_k(\mathbf{x}_n) \end{bmatrix} \quad \text{Eq. (15)}$$

$$\mathbf{r_x} = [R(\mathbf{x_1}, \mathbf{x}), R(\mathbf{x_2}, \mathbf{x}), \cdots, R(\mathbf{x_n}, \mathbf{x})]^T \quad \text{Eq. (16)}$$

where the observed response value, basis function and correlation function can be represented by the vector and matrix description, in Eq. (13)-(16). $\mathbf{y}$ is a vector which includes the response value of samples ($n \times 1$), and $\mathbf{f_x}$ is basis function vector of arbitrary design variables (k×1). $\mathbf{r}_x$ is correlation vector which define the relation between unknown point and experimental sample point (n×1). $\mathbf{F}$ is the basis function matrix ($n \times k$).

$$\hat{\boldsymbol{\beta}} = (\mathbf{F}^{\mathbf{T}}\mathbf{R}^{-1}\mathbf{F})^{\mathbf{T}}\mathbf{R}^{-1}\mathbf{y} \qquad \text{Eq. (17)}$$

Then, as shown in Eq. (17), the estimated coefficients of polynomial basis function can be represented in vector form with correlation matrix of samplings of $\mathbf{R}$ ($n \times n$).

The deviation term in Eq. (11) is assumed by a normal distributed Gaussian process, which refers to the bias or uncertainty in the mean prediction with variance of σ_z^2 and mean of zero. It is important to define the deviation term as the covariance relation to consider the relation among sample points, as in Eq. (18), which denotes the influence exerted by two points on each other. In Eq. (18), a correlation matrix, $\mathbf{R}$ can be defined as a correlation function, which is used to interpolate between two points on a Kriging response surface. Therefore, how smoothly the Kriging surrogate model expresses any two points depends on what one is trying to define with the correlation function. The correlation function can be defined in various ways. In our research, we consider a Gauss function as the correlation function, as shown in Eq. (19) (Koehler and Own, 1996). This function deals with the relation between two data sets by scaling their distance exponentially. As can be seen in Eq. (19), when the distance between $\mathbf{x_i}$ and $\mathbf{x_j}$ is further increased, the value of the correlation function approaches zero. In other words, the influence between any two sample points is exponentially decreased.

$$Cov(Z(\mathbf{x_i}), Z(\mathbf{x_j})) = \sigma_z^2\mathbf{R}[R(\mathbf{x_i}, \mathbf{x_j})] \qquad \text{Eq. (18)}$$

$$R(\mathbf{x_i}, \mathbf{x_j}) = \exp\left(\sum_{k=1}^{d} -\theta_k \, | x_i^k - x_j^k |^p\right) \qquad \text{Eq. (19)}$$

$$\sigma_z^2 = \frac{1}{n}(\mathbf{y} - \mathbf{F}\hat{\boldsymbol{\beta}})^T \mathbf{R}^{-1}(\mathbf{y} - \mathbf{F}\hat{\boldsymbol{\beta}}) \qquad \text{Eq. (20)}$$

In Eq. (11), θ_k and p are the parameters to define the correlation function and both are positive real variables. Because these parameters determine the rate of correlation among the sample points, appropriate methods should be used for their accurate prediction. In this study, the value of parameter of p was set to two. However, the optimum parameter of θ_k can be obtained through the Maximum Likelihood Estimation (MLE), which is treated as an optimization problem as in Eq. (21) (Markus and Welch, 1998). The Hybrid Genetic Algorithm (HGA) was employed to solve the optimization problem. After obtaining the optimum parameter of θ_k, the Kriging surrogate equation can finally be defined as Eq. (22).

$$\begin{aligned} \max \quad & L(\theta_k) = -\frac{1}{2}[n\ln(\sigma_z^2) + \ln(\det(\mathbf{R}))] \\ s.t \quad & \theta_j \geq 0 \quad (j = 1, \cdots, k) \end{aligned} \qquad \text{Eq. (21)}$$

$$\hat{y}(\mathbf{x}) = \mathbf{f}_\mathbf{x}^\mathrm{T}\hat{\boldsymbol{\beta}} + \mathbf{r}_\mathbf{x}^\mathrm{T}\mathbf{R}^{-1}(\mathbf{y} - \mathbf{F}\hat{\boldsymbol{\beta}}) \qquad \text{Eq. (22)}$$

We need the initial sample points to construct the Kriging surrogate model. These sample points can be extracted by using a Design of Experiment (DOE) technique. In this study, we employed a Latin Hypercube Sampling (LHS) method, which is well known and suitable for Kriging surrogate model (Iman et al. 1980). The range of each design variable is discretized with same interval. Then, the whole design space is equally divided into subspace. The LHS ensures that the selected sample does not overlap with other samples because only one sample can be located in each subspace. The number of initial sample points that were extracted by LHS can be insufficient to make the accurate Kriging surrogate model. Therefore, In order to improve the accuracy and robustness of the Kriging surrogate model, the additional sampling points are needed depending on the infill criterion. The infill criterion, such as a statistical Mean Square Error (MSE) estimation or Expected Improvement (EI) method was generally used to find and determine where we should add more points to enhance the accuracy of the Kriging surrogate model (Q. Xu et al. 2012). In our study, we employed the MSE estimation as the infill criterion that evaluates the value of statistical MSE every point in the surrogate model and find the point that has the maximum MSE value. It is where the point is the most inaccurate and uncertain. Then, the accuracy of Kriging surrogate model will be improved by adding adaptive sampling point.

After the Kriging surrogate model is constructed, it may be important to validate its accuracy. Therefore, the accuracy of this model should be verified by comparing the exact value from the additional function evaluation and the estimated value from the model. If there is a large discrepancy between the values, the surrogate model has to be refined until the accuracy of the model is sufficiently accurate. In our study, the adaptive sampling using MSE estimation and model validation were iteratively repeated until the value of error is reduced within 2 %.

The **(Table 3)** shows that how many points are computed with CFD to build the surrogate model. As shown in **(Table 3)**, we extracted the initial sampling points of 90 to construct the initial Kriging surrogate model using LHS method and added additional sampling points to refine and enhance the accuracy of surrogate model using maximum MSE estimation. The number of adaptive sampling point and error of surrogate model are listed in **(Table 3)** depending on the apparent wind direction.

4.3 Design optimization framework

(Figure 4) shows the developed design optimization framework for multiple wing sails. In this framework, the flow analysis for the function evaluation of samples and derivative-free design optimization algorithm with Kriging surrogate model are coupled. The samples for constructing Kriging surrogate model were evaluated by the two-dimensional flow analysis to alleviate the large computing costs. A brief description of the design procedure is as follows. We need the initial sample points to construct the Kriging surrogate model. The initial sample points for the Kriging response surface are randomly extracted by using LHS method. The surface geometries and corresponding the two-dimensional computational meshes are automatically generated by the journaling code. In this study, we employed the SU2_CFD solver, which is an unstructured mesh-based CFD flow solution method, to evaluate the aerodynamic performance of these initial sample points. Using the Kriging-based surrogate model and the derivative-free GA optimization method, we searched for the optimal candidate that maximizes the average thrust coefficient of multiple wing sails. This optimal candidate was validated by making a comparison between the exact value from SU2_CFD, which is the computational analysis and the estimated value from Kriging surrogate model. If differences between the estimated and validated performances are sufficiently small, the design optimization is terminated. Otherwise, the validated optimum is considered to be an additional point, and the response surface is reconstructed. This design procedure proceeds iteratively to find the optimal solution.

5. Aerodynamic characteristics of wing sails

5.1 Grid converge study

The numerical solution computed by CFD involves modeling error and numerical error. The modeling error results from the use of simplified model to consider the effect of real flow physics, such as turbulence model, wall function, and so on. Meanwhile, the numerical error is due to discrete nature of the numerical model, such as grid, time steps, convergence, digits, and so on (Ignazio Maria Viola et al., 2013).

To obtain the numerical solutions using CFD, the flow domain has to be divided into a number of elements, and these elements are called grid or mesh. The accuracy level of solution obtained by CFD depends on the quality and resolution of grid. The simulation results with the coarse grid may not be able to capture the complex flow physics such as wake and separated flow region and large discontinuity in flow variables such as strong shock. On the other hand, the fine grid can give more accurate solution that is similar with real flow physics. However, it requires large computing resources. Therefore, a grid convergence study was conducted to obtain grid independent solution by varying the resolution of grid. In this study, we used the NACA 0012 airfoil and wing with aspect ratio of two for two and three-dimensional CFD analysis. The angle of attack and Reynolds number are set to two degree and 10,000,000, respectively. The six different resolution grids were used to investigate the grid convergence of two and three-dimensional CFD analysis. The number of element and node of each grid is listed in **(Table 4).** As you can see in **(Figure 5)**, as the number of grid increase, the predicted aerodynamic coefficient are broadly similar and converge towards a specific value. The grid convergence study shows that we have to use at least the resolution level of grid corresponding to case4 that can give the grid independent solution in two and three-dimensional CFD analysis.

5.2 CFD Validation

In order to examine the computational accuracy of the CFD flow solver, we performed a solver validation. We confirmed the accuracy of the solver by comparing the results of a two-dimensional numerical analysis and the experimental data (Abbott and von Doenhoff, 1959). As a validation model, we used the NACA 0012 airfoil, which is a symmetrical and no-camber type of the 4-digit series of NACA airfoils. For the solver validation, a 2-D mixed grid was generated, as shown in **(Figure 6).** The size of far-field is 20 times of the airfoil chord length and the height of first cell was adjusted to satisfy the value of y+ close to unity near the solid wall. The total numbers of nodes and elements of the computational mesh are listed in **(Table 1).**

In **(Figure 7),** although the drag coefficients predicted by the numerical analysis differed slightly from the experimental drag coefficients, the lift coefficients are considerably similar until an angle of attack of 16°. In addition, even though the numbers of drag counts have differences, the trends are very similar. Therefore, it is expected that the flow characteristics can be captured using the CFD flow solver. Thus, the results of the numerical analysis are sufficiently accurate.

5.3 Aerodynamic characteristics of multiple wing sails

In order to investigate the effect of the flow interaction, which has a significant effect on the aerodynamic performance of multiple wing sails, we performed a three-dimensional numerical aerodynamic analysis for multiple wing sails by varying the apparent wind direction from 15° to 165° in intervals of 15°. Even though the apparent wind direction varied, the angle of attack of each wing sail, which is a relative angle between the direction of chord line and apparent wind direction, was fixed at 8°. The angle of attack of 8° was also the baseline condition for design optimization. As mentioned before, the single wing sail is a rectangular wing with an aspect ratio of two. The two-dimensional cross sectional shape is NACA 0012 airfoil with and without a trailing edge flap, which can be deflected up to 15°. The length of the flap is 20 % of the chord length. In the numerical simulation, the governing equation is iteratively solved until the error approaches zero. As shown in **(Figure 8)**, all of the steady-state flow solutions were converged and satisfied the convergence criterion that the density-based residual has to be reduced below 10^{-5}.

As indicated in **(Figure 9)**, the thrust performance of multiple and single wing sail with the flap is superior to those without the flap because of the camber effect of the flap. If we employ the trailing edge flap, the effective camber of the airfoil is increased, and the pressure gradient from the stagnation point to the suction peak point is increased. This results in increased velocity at the suction peak (low-pressure region on the upper surface), which causes a larger pressure difference between the upper (leeward side) and the lower (windward side) surface of the wing sail. For these reasons, the single and multiple wing sails with the flap can have better aerodynamic performance than those without the flap.

The multiple wing sails have an arrangements in a row, then the flow interaction occurs among them. Therefore, we confirmed how much thrust is increased or decreased by the flow interaction in multiple wing sails. For investigating the flow interaction effect in the multiple wing sails, we also carried out the aerodynamic analysis for the single wing sail. As a results, the thrust coefficients of the multiple wing sails with and without the flap were smaller by about 21~43 % and 24~37 % respectively than those of the single wing sail. From these results, we can conclude that the flow interaction among the wing sails results in decreased the overall aerodynamic performance of wing sail system. The averaged thrust coefficients of multiple wing sails are lower than that of a single wing sail at all apparent wind directions due to the flow interaction. However, in the multiple wing sails, the average thrust coefficient is divided by the total area of the wing sails. Therefore, the total area should be considered to obtain the total thrust force. Then, the total thrust force of multiple wing sails is about three times that of a single wing sail. Furthermore, the maximum thrust force is generated in the apparent wind direction of 90° because the wing sails in the wind direction of 90° have little flow interaction with each other as compared to those in the other wind directions.

The mechanism of the flow interaction that causes the decreased aerodynamic performance of multiple wing sails is as follows. If the wing sail is set with a positive angle of attack, a stagnation point is located on the lower surface of the wing sail instead of at the leading edge. Furthermore, a suction peak point, which is a low pressure region, is located on the upper surface of the wing sail. The front wing sail, which is located on further upstream direction depending on the incoming apparent wind direction (In case of the apparent wind direction of 45°, the wing sail #1 is the front wing sail and wing sail #2 and #3 are the rear wing sail. However, in case of the apparent wind direction of 135°, the wing sail #3 is the front wing sail and the wing sail #1 and #2 are rear wing sails) causes the stagnation point of the rear wing sail to shift toward the leading edge. It is called “the header effect.” Then, the strength of the suction peak point of the rear wing sails is considerably reduced. Because the pressure gradient from the stagnation point to the suction peak point is also decreased, the flow velocity is less accelerated (the suction peak velocities are reduced). For these reasons, on the upper surface of the rear wing sail, the recovery adverse pressure gradient is also lower. As a result of the above, although the each angle of attack of the multiple wing sails is set to be the same, the effective angle of attack of the rear wing sail is reduced because of the flow interaction effect (Gentry, 1971).

6. Design application and results

6.1 Design optimization problem

In the previous study, we considered only the angle of attack of each wing sail as design variables without the geometric deformation of the wing sails and set the initial angle of attack at 12° (Lee, 2012). However, this initial angle of attack is too high to find a steady-state solution because it causes flow separation on the front wing sail, which was the first wind sail based on the incoming apparent wind direction. Therefore, in this study, 8° was chosen as the initial angles of attack of each wing sail. The angle of attack is the relative angle between the direction of chord line and the direction of apparent wind. We also found both the optimal shape of flap geometry and operating condition for multiple wing sails that are comprised of three wing sails. Therefore, a total of nine design variables are employed, including the flap length, deflection angle, and angle of attack each wing sail. The flap length and deflection angle of baseline were set at 20 % of the chord length (2 m) and 15°, respectively. **(Figure 10)** shows a schematic diagram of the design variables for the design optimization of the multiple wing sails. Constraints on the design variables, called design bounds, were set from 15° to –15° (angle of attack), from 5° to 25° (flap deflection angle), and from 0.5 m to 3 m (flap deflection length).

6.2 Design optimization results based on the two-dimensional flow analysis

In this research, we found the optimal geometric shapes and operating condition of multiple wing sails by varying the apparent wind direction. The design optimization of multiple wing sails is based on the two-dimensional flow analysis. As mentioned before, we considered a total of nine design variables, which included the angle of attack, flap deflection length, and deflection angle of each wing sail. A total of 90 sample points, which were extracted by using LHS method, were estimated using two-dimensional flow analysis for constructing the Kriging surrogate model. In addition, some adaptive sampling procedures and the regeneration of the response surface were performed to improve the accuracy of the Kriging surrogate model.

6.2.1 Design result at apparent wind direction of 45°

The results of the design optimization are listed in **(Table 5)**. As seen in **(Table 5)**, the three types of design variables were gradually increased. It is notable that the angle of attack of wing sail #1 was decreased, whereas those of wing sail #2 and #3 were increased. **(Figure 11)** shows the pressure contour, streamline, and surface pressure coefficient distribution around the wing sails. As you can see **(Figure 11)**, in a comparison between the baseline and the optimized, the strength of the suction peak on wing sail #1 was decreased slightly. This is because the angle of attack of wing sail #1 was reduced to prevent flow separation at the trailing edge flap. This was also caused by the reduced flap length and angle. The design variables of wing sail #1, which is the first wing sail based on incoming wind direction, were reduced (decreased angle of attack and deflection angle, and shortened flap length) to prevent the flow separation. As a result, the flow separation almost disappeared. On the other hand, in the case of wing sails #2 and #3, each design variable was gradually increased (increased angle of attack and deflection angle, and lengthened flap length) to compensate for the angle of attack reduction by the flow interaction. As a result, as compared with the baseline, the aerodynamic performance of all the wing sails was improved. In **(Figure 11)**, compared to baseline, the strengths of the suction peaks of wing sail #2 and #3 were increased. In addition, the surface pressure differences between the upper and lower surface of wing sail #2 and #3 were significantly increased.

In the **(Figure 11)**, we can clearly confirm the header effect that results from the flow interaction among the wing sails. On the baseline results, from wing sail #1 to wing sail #3, the location of the stagnation point gradually moved toward the leading edge of each wing sail because of the flow interaction. Then, the effective angles of attack were gradually decreased. This phenomenon contributed to the strength of the suction peak and the flow separation. A larger effective angle of attack led to stronger suction peak and earlier flow separation. In a comparison of the baseline and optimized flow fields, the stagnation point of the optimized wing sail #2 and #3 shifted from the leading edge to the lower surface that result in increased the effective angle of attack of them. As a results, the flow separation disappeared in the optimized wing sail #1 and the aerodynamic performance was improved in the optimized wing sail #2 and #3 by changing the angle of attack, flap length and deflection angle

6.2.2 Design result at apparent wind direction of 90°

As you can see in the **(Table 5)**, in the apparent wind direction of 90°, because a weak flow interaction occurred, we could not confirm a distinct design trend. Therefore, the design variables of each wing sail were varied independently to improve the aerodynamic performance. The overall angles of attack of the wing sails were increased to enhance the aerodynamic performance. For wing sail #2, the flap deflection length is very small in comparison with the other wing sails. Therefore, to compensate for the shorter deflection length, the angle of attack and deflection angle of wing sail #2 are considerably greater than those of the other wing sails. As a result, we obtained an improvement in the aerodynamic performances of the wing sails that was caused by changing the angle of attack and flap condition.

6.2.3 Design result at apparent wind direction of 135°

The trend of design variables at the apparent wind direction of 135° was found to reverse the trend of design variables at the apparent wind direction of 45°, because wing sail #3 is the first wing sail instead of wing sail #1. However, the angle of attack of the front wing sail (wing sail #3) that is located further upstream side based on the direction of incoming wind slightly increased. Thus, it is thought that relatively less flow interaction occurred in the apparent wind direction of 135° compared to that of 45°. As a result, the angle of attack, deflection length, and angle of attack of the rear wing sail, which is located further downstream side (wing sail #1 and #2), were gradually increased to compensate for the header effect.

The thrust coefficient of the baseline and optimized results are plotted in **(Figure 12)** and listed in **(Table 6).** As a results, we were able to obtain an overall improvement of the averaged thrust approximately 14 ~ 22 % depending on the apparent wind direction, which are very successful design results. The improvements in the averaged thrust are similar in the wind directions of 90° and 135°. The improvements of averaged thrust are the largest in the case of the wind direction of 45°. However, these are design results based on the two-dimensional flow analysis. Therefore, the design results should be validated and verified by the three-dimensional analysis

6.3 Validation of design results using three-dimensional flow analysis

The design results were based on a two-dimensional analysis. A three-dimensional CFD analysis was carried out to validate the design results and to determine whether the design results achieved with the two-dimensional assumption were preserved. We generated a full three-dimension computational grid using the same topology and size with **(Figure 3).** The numbers of nodes and cells in the grid were 1,217,710 and 6,541,622 respectively. The same flow conditions were used in the three-dimensional analysis as used in the two-dimensional analysis.

In **(Table 7)** and **(Figure 12)**, the validation results show that the average thrust performance of optimized multiple wing sails was improved in all wind directions in comparison with the baseline multiple wing sails. We got the thrust improvement of 10 ~ 17 % depending on the apparent wind direction in full three-dimensional flow analysis. Compared to the predicted improvement in two-dimensional analysis, the thrust improvement in three-dimensional analysis has become slightly lower. This means that even though the angle of attack was set to be the same (8°) in the two- and three-dimensional analyses, the flow characteristics around the multiple wing sails were slightly different because of the 3-D effect. In the aerodynamic characteristics of aircraft, a geometrical finite wing causes a "3-D effect", in other words, "a wing-tip vortex". This is driven by the pressure difference between the upper and lower surfaces at the wing tip. In general, the fluid moves from a high-pressure region to a low-pressure region. If the wing has a positive angle of attack, the high-pressure region is distributed on the lower surface, whereas the low-pressure region is distributed on the upper surface of the wing. Therefore, the fluid moves from the lower surface to the upper surface at the wing tip. This phenomenon generates the vortex, which results in a downwash flow. As a result, the effective angle of attack is reduced around the wing tip because of the downwash flow, which results in decreased lift and increased drag (induced drag). In our study, the aspect ratio of each wing sail is two. The wing sail has a low-aspect ratio. Therefore, the 3-D effect should be considered in design process because the downwash effect of the wing tip vortex is important when the aspect ratio of the wing is relatively low. However, the large computational resources were required for the three-dimensional analysis of multiple wing sails. It took about 24 hours for numerical simulation using the parallel computations with 64 cores (Intel Xeon64 E3-1230 3.2 GHz). Actually, it is practically impossible to apply three-dimensional analysis directly to the design optimization. Therefore, we had no choice but to use the two-dimensional analysis in design process instead of the three-dimensional analysis. This is a one of limitations of our research.

7. Conclusion

In this research, we focused on an aerodynamic analysis and design optimization of multiple wing sails. Prior to the design optimization, we performed an aerodynamic analysis to reveal the effect of flow interaction and to investigate the effect of the flap in the wing sail system. For the aerodynamic analysis, we solved the two- and three-dimensional compressible Navier-Stokes governing equation with the Spalart-Allmaras turbulence model using the SU2_CFD solver. We also used a mixed grid topology to more exactly predict the viscous flow. The results showed that the wing sail with the flap has about 20 ~ 50 % larger lift and drag coefficients than the wing sail without the flap with respect to the angle of attack. In the multiple wing sails, the effect of their interaction should be considered to exactly estimate their thrust performance. Although the angle of attack was fixed as 8°, the thrust coefficient of the multiple wing sails were worse than those of the single wing sail by about 21 ~ 43 % depending on the apparent wind direction, because of the flow interaction. As a results, if the flow interaction occur among the wing sails, the effect angle of attack of rear wing sails that is located further downstream based on incoming appearing wind direction significantly decreased due to the header effects. Therefore, the maximum thrust was generated in the apparent wind direction of 90°, because the wing sails in apparent wind direction of 90° had little flow interaction with each other as compared to those in the other wind directions. Furthermore, we developed the design optimization framework for multiple wing sails that is tightly coupled with the gradient-free optimization method of Genetic Algorithm (GA) and Kriging Surrogate model method. Using the developed design framework, the optimal design variables, including angle of attack, flap deflection length and flap deflection angle were obtained that maximize the averaged thrust performance of multiple wing sails with respect to the apparent wind direction. We carried out design optimization for initial angles of attack of 8°. As a result, we acquired thrust increases of approximately 14 ~ 22 % based on the two-dimensional flow analysis. A CFD analysis was also carried out for complete three-dimensional wing sails to determine whether the thrust improvement achieved from the two-dimensional assumption was preserved. The results showed that the thrust performance of the multiple wing sails was improved by 10 ~ 17 %. Although the thrust increments were reduced because of the 3-D effect, these were still good. Thus, it was concluded that the developed design optimizations based on two-dimensional analysis can be applied to the three-dimensional problems

We plan to conduct advanced research on wing sails that can be applied practically to an actual bulk ship using a stability analysis and structural analysis. Furthermore, future studies will consider various aspects such as the sail-hull interaction effect and the optimization of wing sails in three dimensions using efficient optimization methods. Establishing a wing sail system based on the results of these studies is expected to contribute to the development of more efficient eco-friendly ships.

Acknowledgement

This research was supported by the Climate Change Research Hub of KAIST (Grant No. N11160021) from the EEWS Research Project of the office of KAIST EEWS Initiative.

References

Abbott, I. H. and von Doenhoff, A. E., 1959. Theory of Wing Sections including a Summary of Airfoil Data, Dover Publications, New York

Abt, M. and Welch, W. J., 1998. Fisher information and maximum-likelihood estimation of covariance parameters in Gaussian stochastic processes, The Canadian Journal of Statistics, Vol. 26, No. 1, pp.127-137.

Alonso, J. J. and Colonno, M. R., 2012. Multidisciplinary optimization with applications to sonic-boom minimization, In Annual Review of Fluid Mechanics, Vol. 44, pp.505–526.

Bakhvalov, N. S., 1966. On the convergence of a relaxation method with natural constraints on the elliptic operator, U.S.S.R Computational Math. And Math. Phys., Vol. 6, No. 5, pp.101-135.

Bueno-Orovio, A., Castro, C., Palacios, F. and Zuazua, E., 2012. Continuous adjoint approach for the Spalart–Allmaras model in aerodynamic optimization, AIAA Journal, Vol. 50, No. 3, pp.631-646.

Choi, S., Lee, K., Potsdam, M. M. and Alonso, J. J., 2014. Helicopter Rotor Design Using a Time-Spectral and Adjoint-Based Method, Journal of Aircraft, Vol. 51, No. 2, pp. 412-423.

Colonno, M. R., Naik, K., Duraisamy, K. and Alonso, J. J., 2012. An adjoint-based multidisciplinary optimization framework for rotorcraft systems. 12th AIAA Aviation Technology, Integration, and Operations (ATIO) Conference and 14th AIAA/ISSMO Multidisciplinary Analysis and Optimization Conference.

Dumont, A., Le Pape, A., Peter, J. and Huberson, S., 2011. Aerodynamic Shape Optimization of Hovering Rotors Using a Discrete Adjoint of the Reynolds-Averaged Navier–Stokes Equations, Journal of the American Helicopter Society, Vol. 56, No. 3, pp. 1-11

Eleni, D. C., Athanasios, T. I. and Dionissios, M. P., 2012. Evaluation of the Turbulence Models for the Simulation of the low over a National Advisory Committee for Aeronautics NACA0012 Airfoil, Journal of Mechanical Engineering Research, Vol. 4, No. 3, pp.100-111.

Fedorenko, R. P., 1962. A relaxation method for solving elliptic difference equations", U.S.S.R Computational Math. And Math. Phys., Vol. 1, No. 5, pp.1092-1096.

Fujiwara, T., Hirata, K., Ueno, M. and Nimura, T., 2003. On Aerodynamic Characteristics of a Hybrid-sail with Square Soft Sails, Proceedings of the 13th International Offshore and Polar Engineering Conference.

Fujiwara, T., Hearn, G. E., Kitamura, F. and Ueno, M., 2005. Sail-sail and sail-hull interaction effects of hybrid-sail assisted bulk carrier, Journal of Marine Science and Technology, Vol. 10, No. 2, pp.82-95.

Fujiwara, Y., 1980, About the Eco-ship "Shinaitokumaru", Sci. Ship Vol. 33, No. 12, pp.36-42.

Gentry, A. E., 1971. The Aerodynamic of Sail Interaction, Proceedings for the Third AIAA Symposium on the Aero/Hydronautics of Sailing

Ishihara, M. and Watanabe, T., 1980. Prospect of Sail-Equipped Motorship as Assessed from Experimental Ship 'Daioh', Shipboard Energy Conservation Symposium the Society of Naval Architects and Marine Engineers, pp.191~198.

Jameson, A., 1995. Analysis and Design of Numerical Schemes for Gas Dynamics 1 : Artificial Diffusion, Upwind

Biasing, Limiters and Their Effect on Accuracy and Multigrid Convergence. Int. J. Comp. Fluid Dynamics, Vol. 4, pp.171-218.

Jameson, A., 1995. Analysis and Design of Numerical Schemes for Gas Dynamics 2 : Artificial Diffusion and discrete shock structure. Int. J. Comp. Fluid Dynamics, Vol. 5, pp.1-38.

Jameson, A., Vassberg, J. C. and Shankaran, S., 2010. Aerodynamic–Structural Design Studies of Low-Sweep Transonic Wings, Journal of Aircraft, Vol. 47, No. 2, pp. 505-514

Journel, A. G. and Rossi, M. E., 1988. When Do We Need a Trend Model, Technical Report No. 115

Kanai, A., Uzawa, K. and Ouchi, K., 2011. Performance Prediction of Large Sailing Vessel with Multiple Wing Sails by CFD, Wind Tunnel Test and EPP, Conference Proceedings, JASNAOE

Kim, S. H., Alonso, J. J. and Jameson, A., 2002, Design Optimization of High-Lift Configurations Using a Viscous Continuous Adjoint Method, 40th AIAA Aerospace Science Meeting and Exhibit, AIAA 2002-0844

Koehler, J. R. and Own, A. B., 1996. Computer Experiments, Handbook of Statistics, Elsevier Science, New York, pp.261-308.

Kurganov, A. and Levy, D., 2003. A study on the use of Kriging models to approximate deterministic computer models, ASME 2003 Design Engineering Technical Conferences and Computers and Information in Engineering Conference, Chicago, Illinois, USA, Sep. 2-6, 2003, DETC2003/DAC-48762.

Li, Q., Nihel, Y., Nakashima, T. and Ikeda, Y., 2015. A study on the performance of cascade hard sails and sail-equipped vessels, Ocean Engineering, Vol. 98, pp.23-31.

Li, Q., Nihel, Y. and Ikeda, Y., 2012. A Study on Performance of Cascade of Wing Sails for Sail-equipped Vessels Considering their Aerodynamic Interaction, The 6th Asia-Paciffic Workshop on Marine Hydrodynamics-APHydro2012

Lee, H.J., Jo, Y. M., Choi, S. I., Kwon, J. O. and Ahn, S. M., 2012. Aerodynamic Analysis and Design Optimization of Wing-sails, 2012 Fall Korean Society for Computational Fluids Engineering (KSCFE), pp.351-363.

Lukaczyk, T. W., Palacios, F. and Alonso, J. J., 2012. Response surface methodologies for low-boom supersonic aircraft design using equivalent area distributions, The 12th AIAA Aviation Technology, Integration, and Operations (ATIO) Conference and 14th AIAA/ISSMO Multidisciplinary Analysis and Optimization Conference, Aviation Technology, Integration, and Operations (ATIO) Conferences, AIAA Paper 2012-5705

Matsumoto N., Inoue M. and Sudo M., 1981. Operatic Performance of a Sail Equipped Tanker in Wave and Wind, Second International Conference of Stability of Ships and Ocean Vehicles (STAB), pp. 451-464.

Mavriplis, D. J., 1995. Multigrid Techniques for unstructured meshes, NACA Contractor Report 195070, ICASE

Report No. 95-27

Nakashima, T., Li, Q. and Yasunori, N. A., 2010, Fundamental study of wing sail performance considering interaction effects for motor assisted wind driven vessel, J. Kanasai Soc. Nav. Archit., pp.59-62

Nakashima, Takuji, Yamashita, Yoshiriro, Nihei, Yasunori, Li, Qiao, 2011. A Basic Study for Propulsive Performance Prediction of a Cascade of Wing Sails Considering Their Aerodynamic Interaction, Proceeding of the Twenty-first (2011) International Offshore and Polar Engineering Conference (ISOPE), pp.995-1001.

Nadarajah S. K. and Jameson, A., 2007. Optimum Shape Design for Unsteady Three-Dimensional Viscous Flows Using a Nonlinear Frequency-Domain Method, Journal of Aircraft, Vol. 44, No. 5, pp.1513-1527

Ninami, Y., Ninura, T., Fujiwara, Y. and Ueno, M., 2003. Investigation into Underwater Fine Arrangement Effect on Steady Sailing Characteristics of a Sail Assisted Ship, Proceedings of the 13th International Offshore and Polar Engineering Conference.

Ouchi, K. and Uzawa, K., 2009. Concept Design of Wind Driven Vessel in the Era of Low Carbon Society, Proceedings for 12st Ocean Engineering Symposium, JFEOS & JASNAOE

Ouchi, K., Uzawa, K. and Akihiro, K., 2011. Huge Hard Wing Sails for the Propulsor of Next Generation Sailing Vessels, 2nd International Symposium on Marine Propulsors.

Ouchi, K., Uzawa, K., Akihiro K. and Katori, M., 2013. “Wind Challenger” the Next Generation Hybrid Sailing Vessel, 3rd International Symposium on Marine Propulsors.

Onishi, S., Momoki, T. and Ikeda, Y., 2010. A study on a vessel with multiple flat and hard sails to keep service speed in high winds, The 6th International Workshop on Ship Hydrodynamics IWSH2010

Palacios, F., Colonno, M. R., Aranake, A. C., Compos, A., Copeland, S. R., Economon, T. D., Lonkar, A. K., Lukaczyk, T. W., Taylo, Thomas W. R. and Alonso, J. J., 2013. Stanford University Unstructured (SU2) : An open-source integrated computational environment for multi-physic simulation and design, 51st AIAA Aerospace Sciences Meeting including the New Horizons Forum and Aerospace Exposition, AIAA 2013-0287

Palacios, F., Alonso, J. J., Colonno, M. R., Hicken, J. and Lukaczyk, T., 2012. Adjoint-based method for supersonic aircraft design using equivalent area distributions, 50th AIAA Aerospace Sciences Meeting including the New Horizons Forum and Aerospace Exposition, AIAA Paper 2012-0269

Palacios, F., Alonso, J. J. and Jameson, A., 2012. Shape sensitivity of free-surface interfaces using a level set methodology. 42nd AIAA Fluid Dynamics Conference and Exhibit, AIAA Paper 2012-3341

Pham, D. T., and Jin, G., 1995. A hybrid genetic algorithm, Proc. 3rd World Congress on Expert Systems, Seoul, Korea, Vol. 2, pp.748-757.

Sacks, J., Schiller, S. B. and Welch, W. J., 1989. Design for computer experiments, Technometrics, Vol. 31, pp.41-47

Viola, I. M., Sacher, M., Xu, J. and Wang, F., 2015. A numerical method for the design of ships with wind-assisted propulsion, Ocean Engineering, Vol. 105, pp.33-42.

Viola, I. M., Bot, P. and Riotte, M., 2013. On the uncertainty of CFD in sail aerodynamics. International Journal for Numerical Methods in Fluids, Vol. 72, pp.1146-1164.

White, F. M., 1974. Viscous Fluid Flow, McGraw Hill Inc.

Xu, Q., Wehrle, E. and Baier, H., 2012. Adaptive surrogate-based design optimization with expected improvement used as infill criterion, Journal of Optimization, Vol. 61, No. 6, pp.661-684.

Yoon, S. and Jameson, A., 1988. Lower-Upper Symmetric-Gauss-Seidel method for the Euler and Navier-Storkes equations, AIAA Journal, Vol. 26, No. 9, pp.1025-1026.

Zimmerman, D., Pavlik, C., Ruggles, A. and Armstrong, M. P., 1999. An Experimental Comparison of Ordinary and Universal Kriging and Inverse Distance Weighting, Mathematical Geology, Vol. 31, No. 4, pp.375-390

Table List

Table. 1 The information of two- and three-dimensional reference mesh

Computational mesh		
Topology	2-D mixed mesh	3-D mixed mesh
y+ value	1.03	1.08
The number of node	52,200	1,217,000
The number of element	64,700	6,541,000

Table. 2 Input variables for Genetic Algorithm

Genetic Algorithm	
The number of population	200
The number of generation	1024
Probability of crossover	0.75
Probability of mutation	0.03

Table. 3 The number of sampling points and numerical error of Kriging surrogate model

Apparent wind direction (θ)	**45°**	**90°**	**135°**
The number of initial sampling	90	90	90
The number of adaptive sampling	10	8	11
Error of Kriging surrogate model	1.35%	1.12%	1.49%

Table. 4 The number of node and element for grid convergence study

Grid convergence study				
Case	Two-dimensional grid		Three-dimensional grid	
	The number of node	The number of element	The number of node	The number of element
1	18,267	25,238	131,489	897,121
2	26,039	35,182	228,721	1,011,899
3	35,438	47,260	341,712	1,687,120
4	42,269	67,642	417,221	2,241,021
5	55,401	87,186	564,983	2,981,885
6	64,024	99,952	631,564	3,457,321

Table. 5 Design optimization results of multiple wing sails at the angle of attack of 8 °

Apparent wind direction θ =45°

	Baseline	Wing sail #1	Wing sail #2	Wing sail #3
α (degrees)	8	5.27	10.34	16.03
δ (degrees)	15	9.91	12.45	17.99
X_{flap} (meter)	2	1.76	2.14	2.75

Apparent wind direction θ =90°

	Baseline	Wing sail #1	Wing sail #2	Wing sail #3
α (degrees)	8	8.76	15.50	12.42
δ (degrees)	15	13.55	15.18	10.37
X_{flap} (meter)	2	2.17	0.99	2.42

Apparent wind direction θ =135°

	Baseline	Wing sail #1	Wing sail #2	Wing sail #3
α (degrees)	8	12.67	12.45	8.92
δ (degrees)	15	17.39	8.31	8.68
X_{flap} (meter)	2	2.18	2.10	1.70

Table. 6 Thrust improvement in two-dimensional mulitple wing sails

AWA (θ)	**45°**		**90°**		**135°**	
	$C_{Fx.avg}$	$\Delta C_{Fx.avg}$ (%)	$C_{Fx.avg}$	$\Delta C_{Fx.avg}$ (%)	$C_{Fx.avg}$	$\Delta C_{Fx.avg}$ (%)
Baseline	1.1081	-	1.4927	-	1.0362	-
Optimized	1.3545	22.21	1.7057	14.27	1.1860	14.45

Table. 7 Thrust improvement in three-dimensional mulitple wing sails

AWA (θ)	**45°**		**90°**		**135°**	
	$C_{Fx.avg}$	$\Delta C_{Fx.avg}$ (%)	$C_{Fx.avg}$	$\Delta C_{Fx.avg}$ (%)	$C_{Fx.avg}$	$\Delta C_{Fx.avg}$ (%)
Baseline	0.5462	-	0.9525	-	0.7372	-
Optimized	0.6430	17.72	1.0676	12.08	0.8110	10.02

Figure List

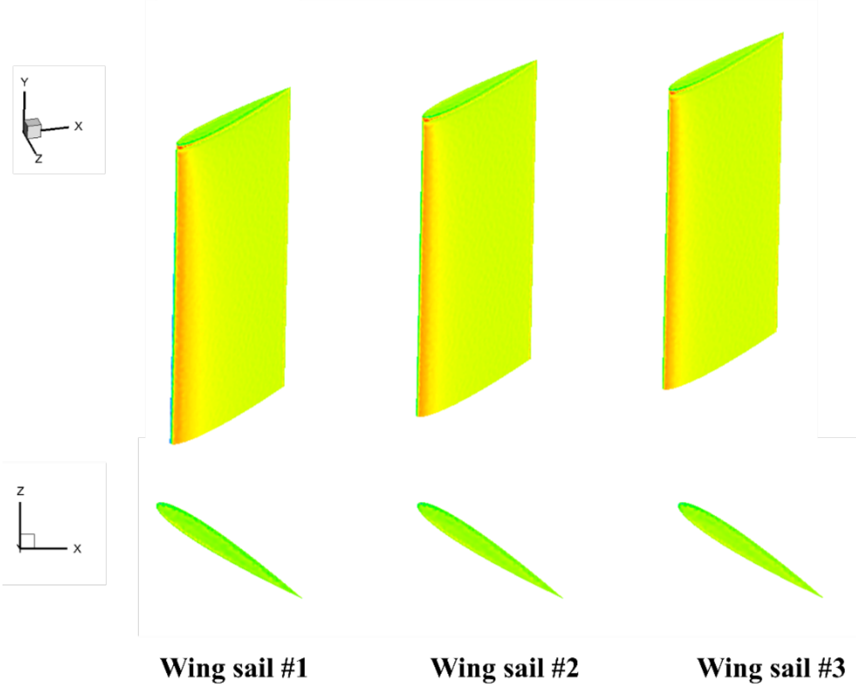

Figure. 1 Schematic view of multiple wing sails

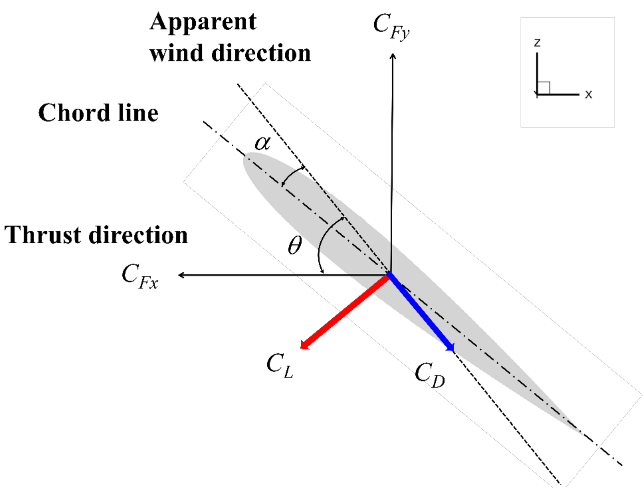

Figure. 2 Relationship between the apparent wind direction and thrust force direction

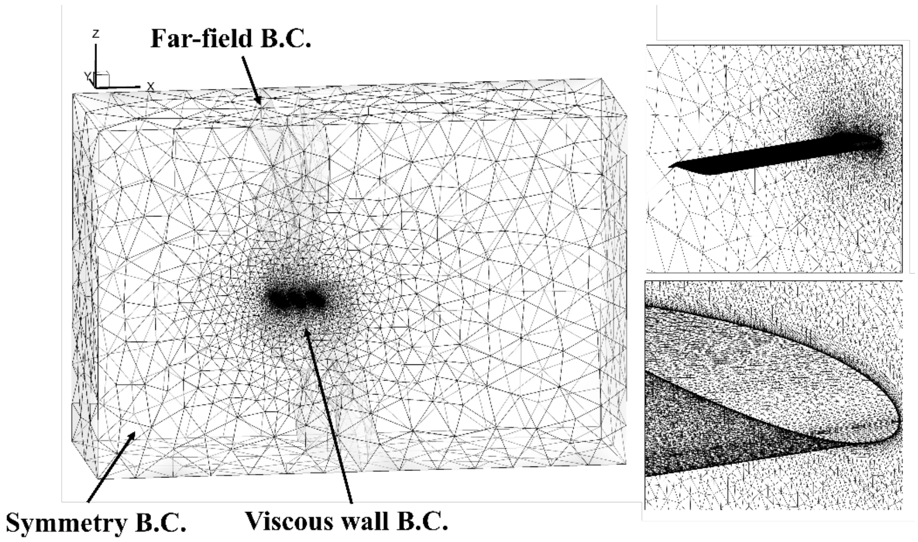

Figure. 3 Computational mesh around multiple wing sails and boundary conditions

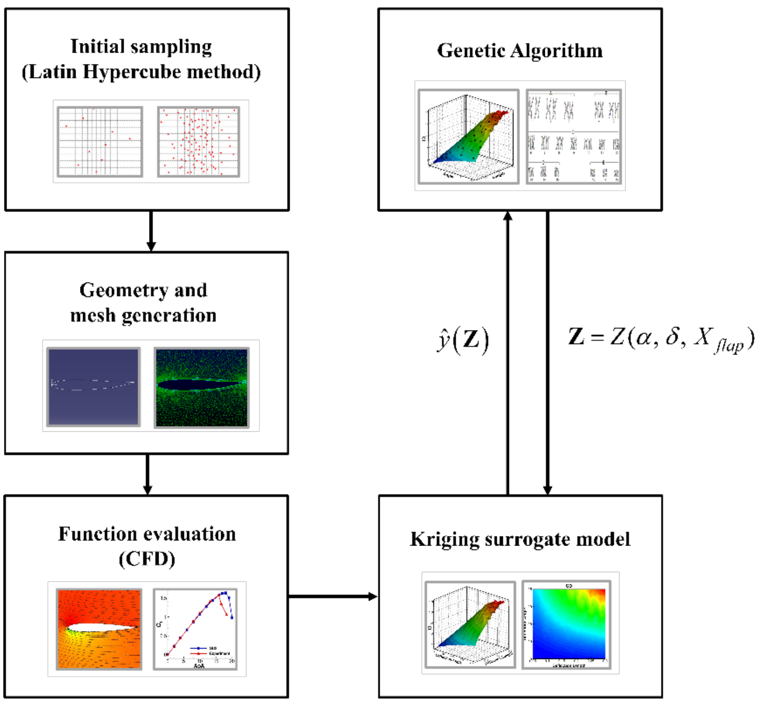

Figure. 4 Design optimization framework for multiple wing sail

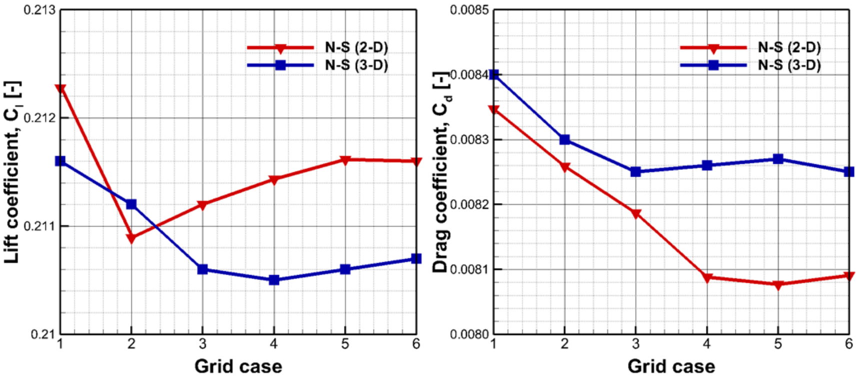

Figure. 5 Grid convergence study for two and three-dimensional flow analysis

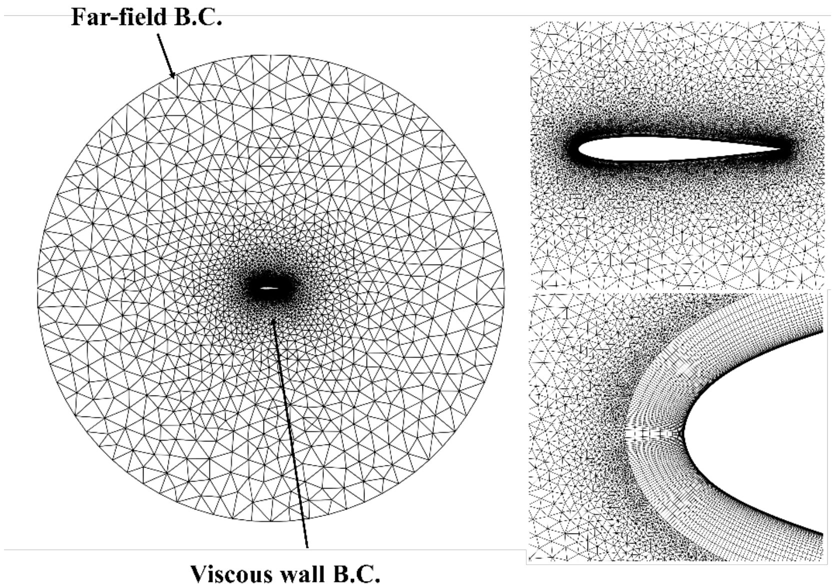

Figure. 6 Computational mesh around NACA0012 airfoil and boundary conditions

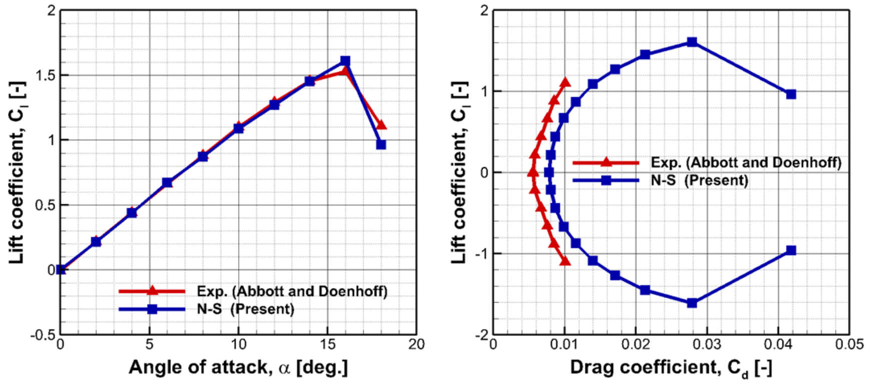

Figure. 7 Aerodynamic coefficients comparison between SU2 and experimental data

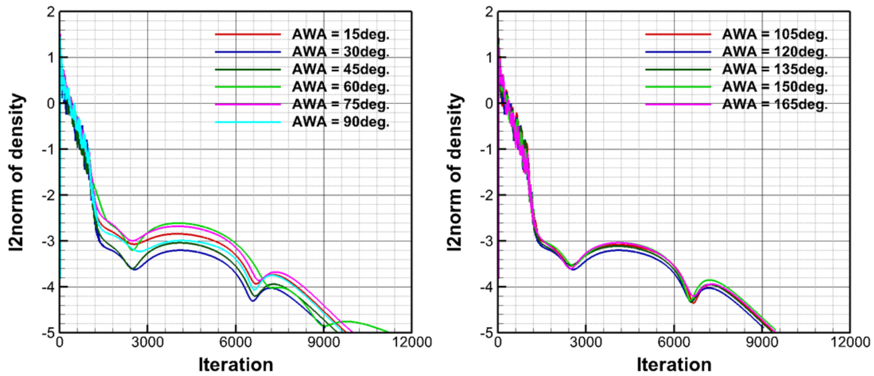

Figure. 8 Convergence history of three-dimensional flow analysis

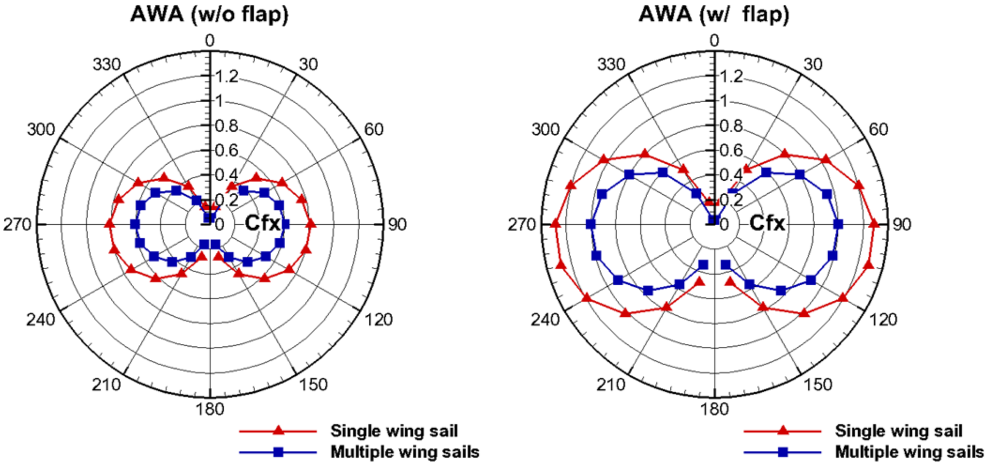

Figure. 9 Thrust force coefficient comparison between single and multiple wing sails

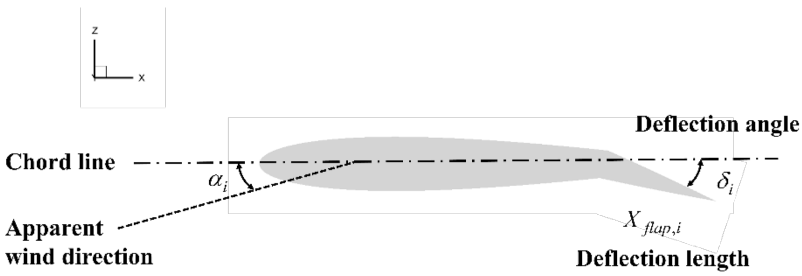

maximize $I = C_{avg,fx}\left(\alpha_i, \delta_i, X_{flap,i}\right)$

by varying $\alpha_i, \delta_i, X_{flap,i} \quad (i = 1,2,3)$

such that

$$\alpha_{lower} \le \alpha_i \le \alpha_{upper}$$
$$\delta_{lower} \le \delta_i \le \delta_{upper}$$
$$X_{lower} \le X_{flap,i} \le X_{upper}$$

Figure. 10 Design variables for design optimization of multiple wing-sails

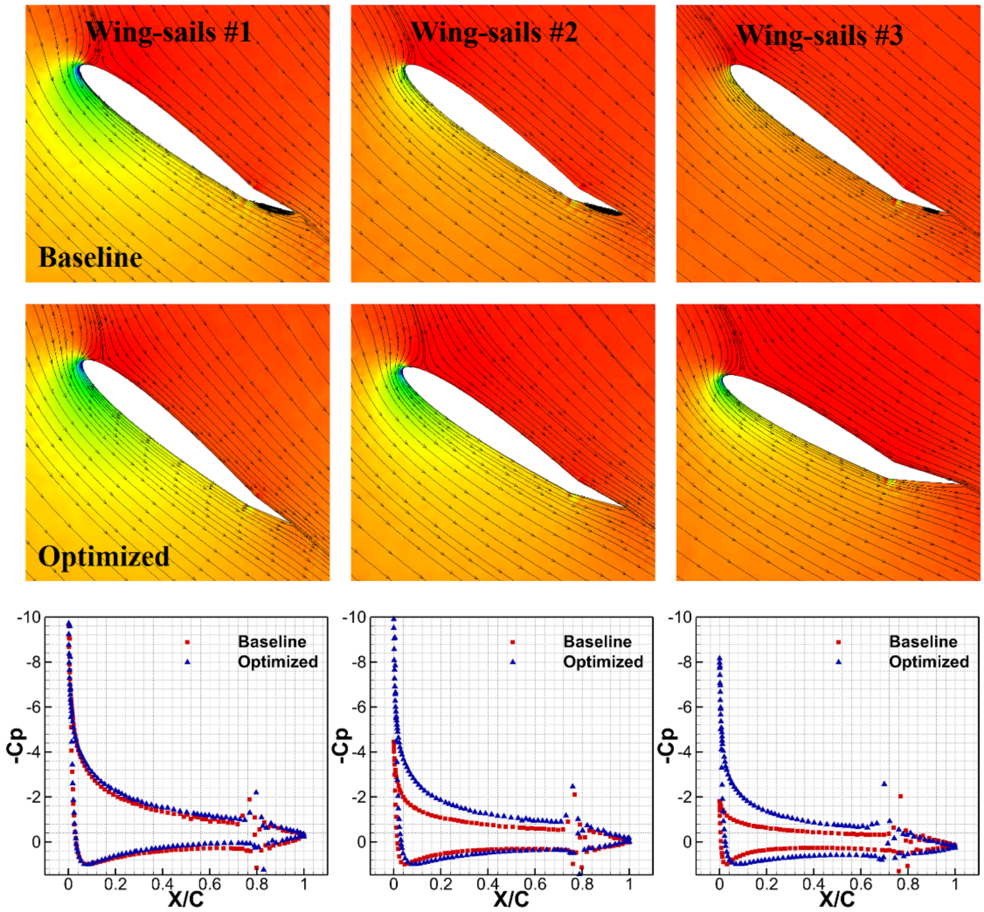

Figure. 11 Flow fields (top, center) and surface pressure distribution (bottom) around baseline and optimized wing sails based on the two-dimensional flow analysis at the AWA of 45°

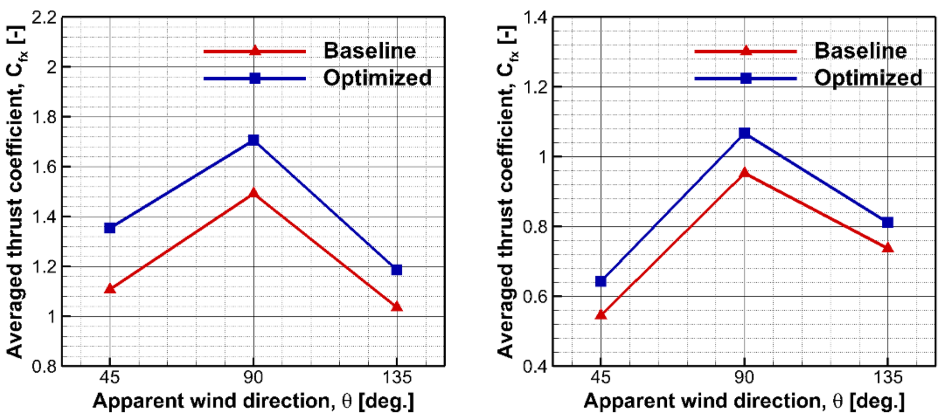

Figure. 12 Thrust force coefficient comparison between baseline and optimized wing sails based on the two (left) and three-dimensional (right) flow analysis